Journal of Sound and Vibration 605 (2025) 118954

Contents lists available at ScienceDirect

Journal of Sound and Vibration

journal homepage: www.elsevier.com/locate/jsvi

3D multimodal inverse method for liner impedance eduction

Hamid Rashidi [a,*], Joachim Golliard [a,b], Thomas Humbert [a]

[a] Laboratoire d'Acoustique de l'Université du Mans (LAUM), UMR 6613, Institut d'Acoustique - Graduate School (IA-GS), CNRS, Le Mans Université, France

[b] Almacoustic, 20 rue Thalès de Milet, 72000, Le Mans, France

ARTICLE INFO

Keywords:
Impedance eduction
Multi-modal acoustic fields
Acoustic liners
Inverse methods
Duct acoustics

ABSTRACT

In aeroacoustic engineering, precise measurements of liner impedance with grazing flow are crucial for optimizing noise reduction strategies. This paper introduces a novel 3D multimodal inverse method designed to educe the acoustic impedance of an acoustic liner in a large duct where many modes can propagate. The cost function is built as the difference between experimental and computed scattering matrices. Without flow, the educed impedance is shown to be in excellent agreement with the impedance measured for similar samples in a small duct where only plane waves propagate. Moreover, the multimodal scattering matrix offers more constraints on the cost function, which improves the method's robustness at high frequencies. This 3D multimodal inverse method is also shown to provide relatively converged results in the presence of flows with mean Mach numbers up to 0.2, holding great promises for improving the design and the optimization of ducted systems in various engineering applications, such as aircraft engines and heating, ventilation, and air-conditioning (HVAC) systems.

1. Introduction

Acoustic liners continue to be the primary technology for reducing the noise emitted by aircraft engines [1]. Their performance is greatly impacted by the conditions within the engines, especially the encountered fast flows and high sound pressure levels [2]. In particular, these factors alter the effective liner acoustic impedance seen by the waves [3]. Thus, precise impedance models and liner optimization methodologies require liner characterizations in experimental facilities where the aeroacoustic conditions are close to those encountered in aircraft engines.

In general, acoustic liners are described by their impedance, defined at the surface as the ratio between the acoustic pressure and the normal velocity, as it does not depend on the cross-section of the used experimental duct. Typical impedance eduction experiments are concerned with the evolution of the impedance as a function of the flow velocity and the incident sound pressure. The experimental techniques used to that end can be classified into two main categories:

- **Inverse Methods**. These methods start in general with an initial guess of the liner's impedance, and they employ both experimental measurements and numerical/analytical models that are encompassed in a cost function that is minimized by the actual liner impedance. This cost function is defined as the difference between the measured and the computed parameters, such as insertion loss [4], acoustic pressure at specific locations [5], acoustic wavenumber [6], scattering matrix [7], etc. Various models can be used to simulate the acoustic field, such as the Convected Helmholtz Equation (CHE) [8], Linearized Euler Equations (LEE) [8] or Linearized Navier–Stokes Equations (LNSE) [3].

* Corresponding author.
E-mail address: Hamid.Rashidi@univ-lemans.fr (H. Rashidi).

https://doi.org/10.1016/j.jsv.2025.118954
Received 19 August 2024; Received in revised form 7 January 2025; Accepted 14 January 2025
Available online 22 January 2025
0022-460X/© 2025 The Authors. Published by Elsevier Ltd. This is an open access article under the CC BY license (http://creativecommons.org/licenses/by/4.0/).

Nomenclature

$\mathbf{A}$, $\mathbf{B}$	Modal amplitudes in the direction of or against the flow, respectively.
$\alpha_m = m\pi$	Transverse wavenumbers in rigid sections.
$\beta_n = n\pi H/W$	Vertical wavenumbers in rigid sections.
c_0	Speed of sound.
C_L	Normalization matrix.
f	Frequency.
H	Duct dimension perpendicularly to the liner.
j	Imaginary number.
$K_{mn}^{\pm}$	Axial wavenumbers in the rigid duct sections.
K_Y	Axial wavenumbers in the lined section.
$\mathbf{\Lambda}$	Amplitude matrix, for normality of modal basis.
(m, n)	Integers associated to transverse (y-axis) and vertical (z-axis) modes.
M	Number of modes in the cost function for impedance eduction.
M_a	Mach number.
N	Number of modes for the acoustic field computation.
Ω	Helmholtz number defined as $2\pi f H/c0$.
$p(x, y, z, t)$	Acoustic field in Cartesian coordinates (x, y, z) as a function of time t.
$\mathbf{P}$	Vector quantity for the acoustic pressure field.
$\mathbf{\Psi}$	Eigenfunctions in the rigid duct.
$\mathbf{Q}$	The derivative of $\mathbf{P}$ according to x.
S, $T^{\pm}$, $R^{\pm}$	Scattering matrix S made of the transmission (T) and reflection (R) matrices.
(u), (d), (y)	Indices indicating the duct sections: upstream, downstream, lined.
W	Width of the duct.
Y	Admittance of the lined wall.
Z	Impedance of the lined wall.

- **Direct Methods**. These methods involve flush-mounted microphones positioned within the test section at regular intervals to capture the evolution of the acoustic field. Then, algorithms inherited from the Prony method are used to extract accurately at least one axial wavenumber [9]. Using the dispersion relation, the transverse wavenumber is also determined, ultimately leading to the calculation of impedance. To that end, the majority of impedance direct eduction methods [10–13] rely on the assumption of a uniform mean flow and the Ingard–Myers boundary condition [14,15], whereas others assume a sheared mean flow and use the Pridmore Brown Equation [16,17] or Linearized Euler Equations (LEE) [18].

This study focuses on implementing an inverse method based on a 3D multimodal calculation of the acoustic field in the presence of a uniform flow. The purpose is to obtain a robust eduction method tailored for a large duct where numerous modes are present. In fact, most of the existing research mentioned above concerns small ducts where only plane waves propagate. However, this situation differs significantly from an engine where most of the acoustic energy is carried by high-order modes due to the width of the nacelles leading to high Helmholtz numbers and the rotating nature of the blade-associated noise sources. These situations have been mainly explored with direct methods [19,20]. Despite promising and interesting results, poor accuracy in the presence of flow noise or if the attenuation is weak can be seen. This is also the conclusion brought when comparing with flow direct and inverse eduction methods in the NASA Curved Duct Test Rig (CDTR) which has 19 modes cut-on at 3 kHz [21]. However, such duct facilities that allow impedance eduction in the presence of multiple cut-on modes, similar to engine conditions, are relatively rare. This gap motivated the present study conducted at the MAINE Flow facility, where up to 19 modes are considered at the highest frequencies, and each can be controlled independently.

This article follows the subsequent structure. First, the multimodal method used for the computation of the 3D acoustic field in the presence of uniform flow is fully described. In particular, the continuity of the acoustic pressure and the acoustic velocity at the liner interfaces are used to formulate the scattering matrix of a duct section with one lined wall. Then, the main characteristics of the experimental facility used in this study are recalled. This permits the introduction of the present inverse eduction method based on the minimization of the difference between the measured scattering matrix and the one computed by the 3D multimodal approach. Finally, the educed impedance is displayed and discussed for two liners. Without flow, these results exhibit excellent agreement with measurements conducted in a small section duct, demonstrating the method's capacity to evaluate the impedance accurately. Moreover, it is demonstrated that this type of inverse method based on the scattering matrix gains a lot of robustness in large ducts since many modes can be used in the optimization process. Finally, consistent results are obtained in the presence of flows up to mean Mach numbers of 0.2, where the uniform flow hypothesis is known to be still valid [18].

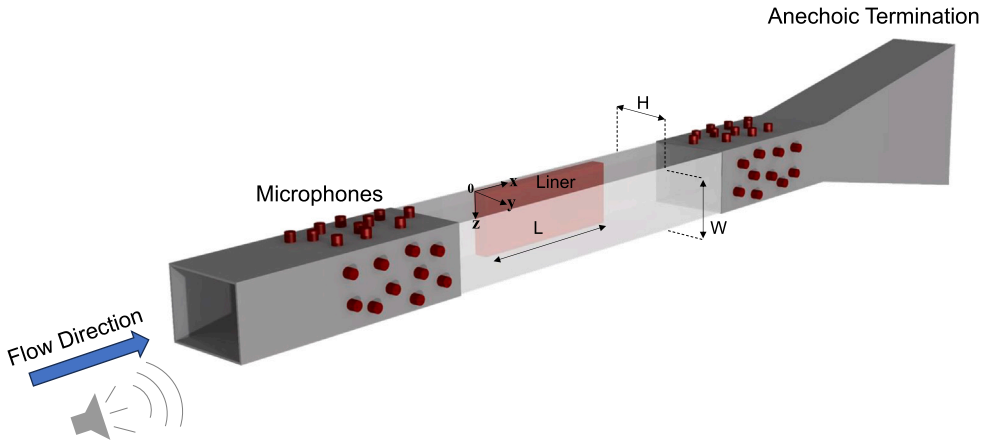

Fig. 1. Schematic of the model duct of section $H \times W$. A lined section of length L is placed between two hard-wall sections in the presence of uniform flow. On both sides of the test section are randomly displayed microphones that are used in the experimental set-up to compute the scattering matrix of the liner sample. The first step of the Multimodal Method is illustrated, with upstream acoustic excitation and the downstream end of the system considered anechoic.

2. Inverse method

The present inverse eduction method uses two components. On one side, the multimodal scattering matrix of the sample is measured in a large duct facility. On the other side, given an impedance value, the acoustic field in the duct is computed, leading to the numerical scattering matrix. This section introduces the numerical method employed to that end and starts by describing the equations and the multimodal method used to calculate the acoustic field in a 3D duct with uniform flow. In particular, the scattering matrix of the lined section is expressed as a function of quantities that can be computed when the impedance is known. Finally, the number of modes needed for the computation to be converged is assessed.

2.1. Multimodal method

The proposed 3D Multimodal Method is based on the 2D method introduced in [7]. It consists mainly of the projection of the propagation equation on a complete basis of orthogonal functions composed of the rigid duct modes. The configuration of the problem considered is shown in Fig. 1.

The acoustic field $p(x, y, z, t)$ in such a 3D waveguide follows the Helmholtz equation

$$\frac{\mathrm{D}^2 p}{\mathrm{D}t^2} - \frac{\partial^2 p}{\partial x^2} - \frac{\partial^2 p}{\partial y^2} - \frac{\partial^2 p}{\partial z^2} = 0, \tag{1}$$

where the convective derivative reads, in the hypothesis of a uniform flow defined by the mean Mach number M_a,

$$\frac{\mathrm{D}^2}{\mathrm{D}t^2} = \left(\mathrm{j}\Omega + M_a \frac{\partial}{\partial x}\right)^2. \tag{2}$$

$\Omega = 2\pi f H / c_0$ is the non-dimensional frequency (also called Helmholtz number) based on the height of the duct H, the speed of sound c_0, and the frequency f. The axes x and y are made dimensionless by H, and the duct is divided into three parts. Two of them have four rigid walls, while one wall ($y = 0$) of the middle part is lined. All three sections are defined by their admittance, i.e. the inverse of the impedance, which equals 0 everywhere for the hard wall sections and $Y(x)$ for the lined wall. On the latter, the boundary condition that expresses the pressure and displacement continuities at the treated wall is the Ingard–Myers boundary condition [14]:

$$\left.\frac{\partial p}{\partial y}\right|_{y=0} = \frac{\mathrm{D}^2}{\mathrm{D}t^2}\left(\frac{-Y(x)p(x,0,z)}{\mathrm{j}\Omega}\right). \tag{3}$$

Then, the pressure field $p(x, y, z)$ given these boundary conditions is searched as a modal combination of the form

$$p(x, y, z) = \sum_{m,n=0}^{+\infty} \Psi_{mn}(y, z) P_{mn}(x), \tag{4}$$

or $p(x, y, z) = \mathbf{\Psi}(y, z)\mathbf{P}(x)$ with matrices. The functions

$$\Psi_{mn} = \Lambda_{m,n} \cos\left(\alpha_m y\right) \cos\left(\beta_n z\right) \tag{5}$$

are solutions of Eq. (1) in the rigid channel and (m, n) are integers. Finally, the amplitude matrix $\mathbf{\Lambda}$ made of the coefficients $\Lambda_{m,n}$ reads

$$\Lambda = \sqrt{\frac{H}{W}} \begin{pmatrix} 1 & \sqrt{2} & \sqrt{2} & \dots \\ \sqrt{2} & 2 & 2 & \dots \\ \sqrt{2} & 2 & 2 & \dots \\ \vdots & \vdots & \vdots & \ddots \end{pmatrix}, \tag{6}$$

in order to ensure the normality of the modal basis.

Once the modal basis is defined, the aim is to rewrite the Helmholtz equation under a form that can be solved numerically. To that end, Eq. (1) is projected onto the rigid duct modes Ψ_{mn}:

$$\int_0^{\frac{W}{H}} \int_0^1 \frac{\mathrm{D}^2 p}{\mathrm{D}t^2} \Psi_{mn} \,\mathrm{d}y \,\mathrm{d}z - \int_0^{\frac{W}{H}} \int_0^1 \frac{\mathrm{D}^2 p}{\mathrm{D}x^2} \Psi_{mn} \,\mathrm{d}y \,\mathrm{d}z - \int_0^{\frac{W}{H}} \int_0^1 \frac{\mathrm{D}^2 p}{\mathrm{D}y^2} \Psi_{mn} \,\mathrm{d}y \,\mathrm{d}z - \int_0^{\frac{W}{H}} \int_0^1 \frac{\mathrm{D}^2 p}{\mathrm{D}z^2} \Psi_{mn} \,\mathrm{d}y \,\mathrm{d}z = 0. \tag{7}$$

By expanding each of the four integral terms, Eq. (7) becomes

$$-\Omega^2 \mathbf{P} + M_a^2 \frac{\partial^2 \mathbf{P}}{\partial x^2} + 2\mathrm{j}\Omega M_a \frac{\partial \mathbf{P}}{\partial x} - \frac{\partial^2 \mathbf{P}}{\partial x^2} + \alpha_m^2 \mathbf{P} + \beta_n^2 \mathbf{P} - \left(\frac{Y(x) C_L}{\mathrm{j}\Omega} \right) \left(\Omega^2 \mathbf{P} - M_a^2 \frac{\partial^2 \mathbf{P}}{\partial x^2} - 2\mathrm{j}\Omega M_a \frac{\partial \mathbf{P}}{\partial x} \right) = 0, \tag{8}$$

where the matrix C_L is given by:

$$C_L = \begin{pmatrix} 1 & \sqrt{2} & \sqrt{2} & \dots \\ \sqrt{2} & 2 & 2 & \dots \\ \sqrt{2} & 2 & 2 & \dots \\ \vdots & \vdots & \vdots & \ddots \end{pmatrix}. \tag{9}$$

Finally, Eq. (8) is written as

$$M_1 \frac{\partial^2 \mathbf{P}}{\partial x^2} = M_2 \frac{\partial \mathbf{P}}{\partial x} + M_3 \mathbf{P}, \tag{10}$$

with:

$$\begin{aligned} M_1 &= (1 - M_a^2) - \frac{Y M_a^2}{\mathrm{j}\Omega} C_L, \\ M_2 &= 2\mathrm{j}\Omega M_a I + 2Y M_a C_L, \\ M_3 &= (\alpha_m^2 + \beta_n^2 - \Omega^2) I + \mathrm{j} Y \Omega C_L. \end{aligned} \tag{11}$$

In matrix form, Eq. (10) reads

$$\frac{\mathrm{d}}{\mathrm{d}x} \begin{pmatrix} \mathbf{P} \\ \mathbf{Q} \end{pmatrix} = \begin{pmatrix} 0 & I \\ M_1^{-1} M_3 & M_1^{-1} M_2 \end{pmatrix} \begin{pmatrix} \mathbf{P} \\ \mathbf{Q} \end{pmatrix}, \tag{12}$$

where $\mathbf{Q} = \frac{\mathrm{d}\mathbf{P}}{\mathrm{d}x}$. I and 0 are, respectively, the identity and zero matrices. The next step consists in computing the eigenvectors X and the eigenvalues λ of the matrix in Eq. (12), leading to the axial wavenumbers in the lined section $K_Y = \frac{\mathrm{j}\lambda}{\Omega}$. Then, λ and X are split into two sets depending on the propagation direction of the waves. When the imaginary part of K_Y is negative, it corresponds to waves propagating in the same direction as the flow: we denote K_Y^+ these wavenumbers and X^+ the associated wavevectors. When the imaginary part of K_Y is positive, it corresponds to waves propagating against the flow: we denote K_Y^- these wavenumbers and X^- the associated wavevectors. When N modes are considered in the computation, the wavenumbers $K_Y^\pm$ are diagonal matrices of size $N \times N$.

2.2. Three zones method for the computation of the acoustic field

In the whole study, the duct is divided into three zones, as depicted by Fig. 2. The waves that propagate in the same direction as the flow have amplitudes $\mathbf{A}$, while the waves propagating against the flow have modal amplitudes $\mathbf{B}$. The upstream and downstream sections, labeled (u) and (d), are made of hard walls, and the wavenumbers $K_{mn}^\pm$ are given by:

$$K_{mn}^\pm = \frac{-M_a \pm \sqrt{1 - (1 - M_a^2)(\frac{\alpha_m^2 + \beta_n^2}{\Omega^2})}}{(1 - M_a^2)}, \tag{13}$$

with $\alpha_m = m\pi$ and $\beta_n = n\pi H/W$ the transverse and vertical wavenumbers. Section (y) has one wall of admittance Y, and the wavenumbers are denoted K_Y. To be able to compute the acoustic field, the unknown modal amplitudes in the three sections are

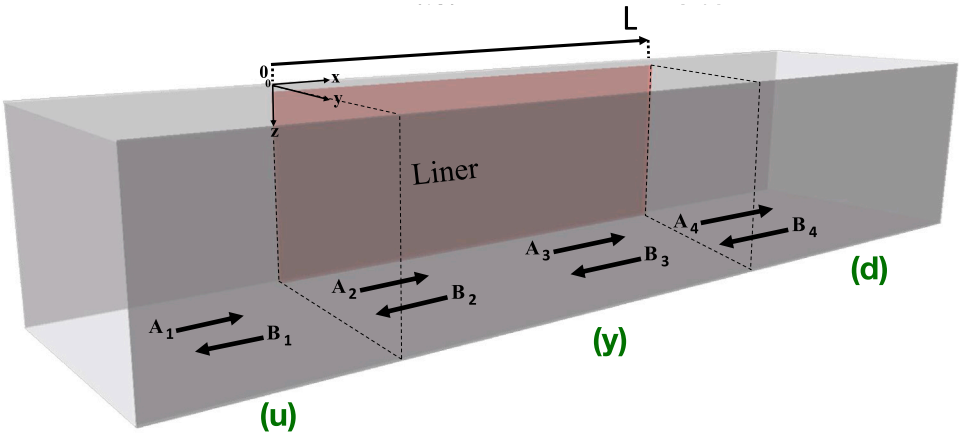

Fig. 2. 3D sketch of the three zones method that includes a lined section (y) and hard wall sections (u) and (d). The modal amplitudes A_1 and B_4 are the amplitude of the incident waves, whereas the other amplitudes are computed.

now expressed as functions of the incident amplitudes $\mathbf{A_1}$ (case of an upstream source, downstream propagation) and $\mathbf{B_4}$ (downstream source, upstream propagation). This is done using the continuity of Eq. (8) at the interfaces between the hard-wall sections and the lined section, as detailed in the following.

First, in the hard-wall sections (u) and (d), the acoustic pressures $\mathbf{P_{(u)}}$ and $\mathbf{P_{(d)}}$ are written:

$$\begin{aligned}\mathbf{P_{(u)}}(x) &= \mathbf{A_1}\exp^{-\mathrm{j}K^+_{mn}\Omega x} + \mathbf{B_1}\exp^{-\mathrm{j}K^-_{mn}\Omega x} \qquad \text{for} \quad x<0,\\ \mathbf{P_{(d)}}(x-L) &= \mathbf{A_4}\exp^{-\mathrm{j}K^+_{mn}\Omega(x-L)} + \mathbf{B_4}\exp^{-\mathrm{j}K^-_{mn}\Omega(x-L)} \qquad \text{for} \quad x>L,\end{aligned} \tag{14}$$

where $\mathbf{A_1}$ and $\mathbf{B_1}$ are column vectors of length N containing the amplitudes of the incident and reflected modes at the upstream interface. At the downstream interface, $\mathbf{A_4}$ are the transmitted modal amplitudes corresponding to an incident field $\mathbf{A_1}$ and $\mathbf{B_4}$ are the modal amplitudes reflected by the duct end. In practice, we will consider $\mathbf{B_4}$ equal to 0 when the incident modes $\mathbf{A_1}$ are imposed from upstream for the downstream-propagation computation. This assumption, equivalent to an assumption of anechoic termination downstream, allows solving for $\mathbf{B_1}$ and $\mathbf{A_4}$ and thus for the full acoustic field in the duct. Similarly, the computation for upstream propagation is performed by imposing the incident modes $\mathbf{B_4}$ from downstream and solving for $\mathbf{B_1}$ and $\mathbf{A_4}$ with anechoic condition upstream ($\mathbf{A_1}$ equal to 0).

In the lined section, the vectors $\mathbf{P_{(y)}}$ and $\mathbf{Q_{(y)}}$ are expressed in terms of the amplitudes $\mathbf{A_2}$ and $\mathbf{B_3} = \mathbf{B_2}\exp^{\mathrm{j}K^-_Y\Omega L}$:

$$\begin{aligned}\mathbf{P_{(y)}}(x) &= \mathbf{A_2}X^+E^+(x) + \mathbf{B_3}X^-E^-(x-L),\\ \mathbf{Q_{(y)}}(x) &= -\mathrm{j}\Omega(\mathbf{A_2}X^+K^+_YE^+(x) + \mathbf{B_3}X^-K^-_YE^-(x-L)),\end{aligned} \tag{15}$$

where $E^{\pm}(x) = \exp^{-\mathrm{j}K^{\pm}_Y\Omega x}$. The choice of amplitudes $\mathbf{A_2}$ and $\mathbf{B_3}$ (and not $\mathbf{A_2}$ and $\mathbf{B_2}$ for example) to express the acoustic field in the lined section is made to avoid divergence problems due to the evanescent modes and possibly strongly attenuated modes in lined section (y).

The method to match the modes between the different regions, based on the continuity of Eq. (8) at the interfaces, is extensively described in [22] for the 2D case, so only the main steps are reminded here.

First, Eq. (8) is written under the form:

$$\begin{aligned}\frac{\mathrm{d}^2}{\mathrm{d}x^2}\left[(M_a^2-1)\mathbf{P} + \frac{Y(x)C_LM_a^2}{\mathrm{j}\Omega}\mathbf{P}\right] &+ \frac{\mathrm{d}}{\mathrm{d}x}\left[2\mathrm{j}\Omega M_a\mathbf{P} + 2\frac{Y(x)C_L}{\mathrm{j}\Omega}\mathrm{j}\Omega M_a\mathbf{P}\right]\\ &+ \left[-\Omega^2(1+\frac{Y(x)C_l}{\mathrm{j}\Omega}) + \alpha_m^2 + \beta_n^2\right]\mathbf{P} = 0.\end{aligned} \tag{16}$$

The admittance $Y(x)$ on the $y=0$ wall is a Heaviside function equal to zero in the rigid sections and Y in the lined section. However, the term associated with the derivative $\mathrm{d}^2/\mathrm{d}x^2$ has to be continuous at the interface. This condition is expressed by the relation:

$$\left[\!\left[(M_a^2-1)\mathbf{P} + \frac{Y(x)C_LM_a^2}{\mathrm{j}\Omega}\mathbf{P}\right]\!\right] = 0, \tag{17}$$

where the brackets $[\![\cdot]\!]$ express the difference between the value of the term just before the interface and its value right after. The other terms of Eq. (16) also have to be continuous, leading to:

$$\left[\!\left[(M_a^2-1)\mathbf{Q} + \frac{Y(x)C_LM_a^2}{\mathrm{j}\Omega}\mathbf{Q} + 2\mathrm{j}\Omega M_a\mathbf{P} + 2\frac{Y(x)C_L}{\mathrm{j}\Omega}\mathrm{j}\Omega M_a\mathbf{P}\right]\!\right] = 0. \tag{18}$$

Then, P and Q as given by Eqs. (14) and (15) for the sections (u) and (y) are introduced in the continuity relations Eqs. (17) and (18). It leads at the first interface ($x = 0$), with $E_L^- = E^-(-L)$ to the following relations:

$$\mathbf{A_1} + \mathbf{B_1} = \Gamma_1(X^+\mathbf{A_2} + X^- E_L^- \mathbf{B_3}), \tag{19}$$

$$\mathbf{A_1}(-\mathrm{j}K_{mn}^+\Omega + \Gamma_2) + \mathbf{B_1}(-\mathrm{j}K_{mn}^-\Omega + \Gamma_2) = \mathbf{A_2}X^+(-\mathrm{j}\Gamma_1 K_Y^+\Omega + \Gamma_3) + \mathbf{B_3}E_L^- X^-(-\mathrm{j}\Gamma_1 K_Y^-\Omega + \Gamma_3), \tag{20}$$

with

$$\Gamma_1 = I - \frac{YC_L M_a^2}{\mathrm{j}\Omega(1-M_a^2)}, \qquad \Gamma_2 = \frac{-2\mathrm{j}\Omega M_a}{(1-M_a^2)}, \qquad \Gamma_3 = \frac{-2\mathrm{j}\Omega M_a}{(1-M_a^2)} - \frac{2YC_L M_a}{(1-M_a^2)}. \tag{21}$$

Finally, Eqs. (19) and (20) are written in a common matrix form while using for the lined section only the amplitudes $\mathbf{A_2}$ and $\mathbf{B_3}$:

$$\begin{pmatrix} I & I \\ -\mathrm{j}K_{mn}^+\Omega + \Gamma_2 & -\mathrm{j}K_{mn}^-\Omega + \Gamma_2 \end{pmatrix} \begin{pmatrix} \mathbf{A_1} \\ \mathbf{B_1} \end{pmatrix} = \begin{pmatrix} \Gamma_1 X^+ & \Gamma_1 X^- E_L^- \\ X^+(-\mathrm{j}\Gamma_1 K_Y^+\Omega + \Gamma_3) & X^- E_L^-(-\mathrm{j}\Gamma_1 K_Y^-\Omega + \Gamma_3) \end{pmatrix} \begin{pmatrix} \mathbf{A_2} \\ \mathbf{B_3} \end{pmatrix}. \tag{22}$$

Similarly, the continuity at the second interface ($x = L$) allows writing, with $E_L^+ = E^+(L)$ the following relation between the acoustic fields in the lined and rigid sections (y) and (d):

$$\begin{pmatrix} I & I \\ -\mathrm{j}K_{mn}^+\Omega + \Gamma_2 & -\mathrm{j}K_{mn}^-\Omega + \Gamma_2 \end{pmatrix} \begin{pmatrix} \mathbf{A_4} \\ \mathbf{B_4} \end{pmatrix} = \begin{pmatrix} \Gamma_1 X^+ E_L^+ & \Gamma_1 X^- \\ X^+ E_L^+(\Gamma_3 - \mathrm{j}\Gamma_1 K_Y^+\Omega) & X^-(\Gamma_3 - \mathrm{j}\Gamma_1 K_Y^-\Omega) \end{pmatrix} \begin{pmatrix} \mathbf{A_2} \\ \mathbf{B_3} \end{pmatrix}. \tag{23}$$

2.3. Scattering matrix computation

The inverse method proposed in this paper is based on the comparison between the experimental and the numerical scattering matrices of the lined section. Using the previously introduced notations, the scattering matrix S links the modal coefficients describing the transmitted and reflected acoustic fields to the incident field according to

$$\begin{pmatrix} \mathbf{A_4} \\ \mathbf{B_1} \end{pmatrix} = S \begin{pmatrix} \mathbf{A_1} \\ \mathbf{B_4} \end{pmatrix} = \begin{pmatrix} T^+ & R^- \\ R^+ & T^- \end{pmatrix} \begin{pmatrix} \mathbf{A_1} \\ \mathbf{B_4} \end{pmatrix}. \tag{24}$$

$T^\pm$ and $R^\pm$ are the transmission and reflection matrices, which reduce to:

$$T^+ = \frac{\mathbf{A_4}}{\mathbf{A_1}}, \qquad R^+ = \frac{\mathbf{B_1}}{\mathbf{A_1}}, \qquad T^- = \frac{\mathbf{B_1}}{\mathbf{B_4}}, \qquad R^- = \frac{\mathbf{A_4}}{\mathbf{B_4}}, \tag{25}$$

when the assumptions of a downstream ($\mathbf{B_4} = 0$) or an upstream ($\mathbf{A_1} = 0$) anechoic termination are made to compute respectively the upstream (T^+ and R^+) or the downstream (T^- and R^-) coefficients. Note that the scattering matrix is intrinsic to the lined duct section and does not depend on the boundary conditions. The hypotheses of anechoic terminations made for the computation do not contradict this but are simply used to simplify the resolution of the problem.

In the numerical framework drawn by this paper, the multimodal formalism permits a straightforward computation of these matrices by using the relations provided by Eq. (22) and (23). This is done by writing the scattering problem at the two interfaces under the form

$$\begin{pmatrix} \mathbf{A_1} \\ \mathbf{B_1} \end{pmatrix} = \begin{pmatrix} x_1 & x_2 \\ x_3 & x_4 \end{pmatrix} \begin{pmatrix} \mathbf{A_2} \\ \mathbf{B_3} \end{pmatrix}, \tag{26}$$

$$\begin{pmatrix} \mathbf{A_4} \\ \mathbf{B_4} \end{pmatrix} = \begin{pmatrix} y_1 & y_2 \\ y_3 & y_4 \end{pmatrix} \begin{pmatrix} \mathbf{A_2} \\ \mathbf{B_3} \end{pmatrix}, \tag{27}$$

where $x_{1\ldots4}$ and $y_{1\ldots4}$ can be computed from Eqs. (22) and (23) respectively. The expressions of these quantities and their computation are given in Appendix A. Then, it is possible to link the amplitudes in both rigid zones by first inverting Eq. (27), so that:

$$\begin{pmatrix} \mathbf{A_2} \\ \mathbf{B_3} \end{pmatrix} = \frac{1}{y_1 y_4 - y_2 y_3} \begin{pmatrix} y_4 & -y_2 \\ -y_3 & y_1 \end{pmatrix} \begin{pmatrix} \mathbf{A_4} \\ \mathbf{B_4} \end{pmatrix}. \tag{28}$$

This expression is substituted in Eq. (26), leading after matrix multiplication to a relation between zone (1) and zone (3) as a function the interfaces coefficients:

$$\begin{pmatrix} \mathbf{A_1} \\ \mathbf{B_1} \end{pmatrix} = \frac{1}{y_1 y_4 - y_2 y_3} \begin{pmatrix} x_1 y_4 - x_2 y_3 & -x_1 y_2 + x_2 y_1 \\ x_3 y_4 - x_4 y_3 & -x_3 y_2 + x_4 y_1 \end{pmatrix} \begin{pmatrix} \mathbf{A_4} \\ \mathbf{B_4} \end{pmatrix}. \tag{29}$$

Some more linear algebra, detailed in Appendix B, is finally required to transform Eq. (29) into the scattering matrix Eq. (24) which links the outputs of the system to the inputs. Achieving this step yields the following expressions for the scattering coefficients:

$$T^+ = \frac{y_1 - \frac{y_2 y_3}{y_4}}{x_1 - \frac{x_2 y_3}{y_4}}, \qquad R^+ = \frac{x_3 - \frac{x_4 y_3}{y_4}}{x_1 - \frac{x_2 y_3}{y_4}}, \tag{30}$$

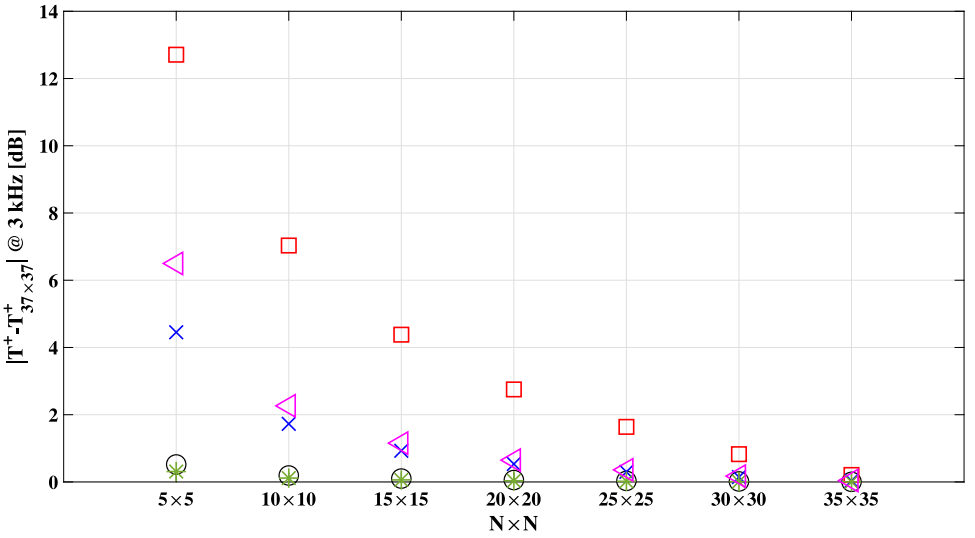

Fig. 3. Difference between the upstream transmission T^+ at 3000 Hz obtained using $N \times N$ projection modes for the calculation and the transmission obtained with 37×37 projection modes. ○: plane wave $(0,0)$. □: horizontal mode$(0,2)$. ×: horizontal mode $(0,3)$. ✻: vertical mode $(2,0)$. ◁: mode $(2,1)$.

$$T^- = \frac{x_4 - \frac{x_3 x_2}{x_1}}{y_4 - \frac{y_3 x_2}{x_1}}, \qquad R^- = \frac{y_2 - \frac{y_1 x_2}{x_1}}{y_4 - \frac{y_3 x_2}{x_1}}. \tag{31}$$

2.4. Numerical evaluation of the 3D multimodal method

In the following, the convergence of the introduced scattering matrix computation is evaluated. To that end, an 80 cm long test section is lined by a non-dimensional impedance Z_t made of a constant resistance equal to 1 and a reactance that corresponds to 30 mm deep cavities:

$$Z_t = 1 - i \cot\left(2\pi f \frac{0.03}{c_0}\right). \tag{32}$$

For each considered frequency, the wavenumbers in the rigid parts are computed using Eq. (13), while the modal content in the lined part is given by the eigenvalues and the eigenvectors of the matrix in Eq. (12). This is sufficient to be able to compute the full scattering matrix through Eq. (30).

The convergence of the multimodal method is assessed at 3000 Hz considering the diagonal of the transmission matrix T^+. This particular frequency has been chosen to provide a significant number of propagating modes. Fig. 3 displays, as a function of the number $N \times N$ of projection modes (for both the horizontal and vertical directions), the absolute value of the difference between the obtained transmission and the one obtained using a projection on 37×37 modes. Five modes are shown, and they have been selected in order to cover all the possible cases: the plane wave, purely horizontal modes, purely vertical modes, and combined modes. For all of these modes, Fig. 3 displays an exponential convergence of the computation, with a decrease of the shown difference that becomes close to 0 when more than 35×35 modes are used for the projection. However, it is worth noting that the convergence speed varies depending on the type of the considered mode. For instance, the transmission coefficient associated with the plane wave converges relatively quickly, as does the mode $(2,0)$, which represents vertical modes. The latter are rigid duct modes, which do not see the liner. In contrast, the horizontal modes $(0,2)$ and $(0,3)$, as well as the mode $(2,1)$, require more time to converge. This can be attributed to the need for a greater number of modes to adequately describe the energy transfer between the modes induced by the presence of the liner.

3. Experimental set-up characteristics and measurement method

The second part of the proposed liner eduction method relies on the measurement of the scattering matrix of the liner sample. This is done in the MAINE Flow facility and the present section describes both the test rig and the related experimental techniques. Finally, the inverse method that permits the computation of the liner impedance, given its scattering matrix, is described.

3.1. MAINE flow facility

The MAINE Flow test rig (see Fig. 4) is designed to reproduce conditions that acoustic liners encounter in an aircraft engine. In particular, the flow can reach a mean Mach value of 0.63 in the test section. The dimensions of the cross-section are 280 mm

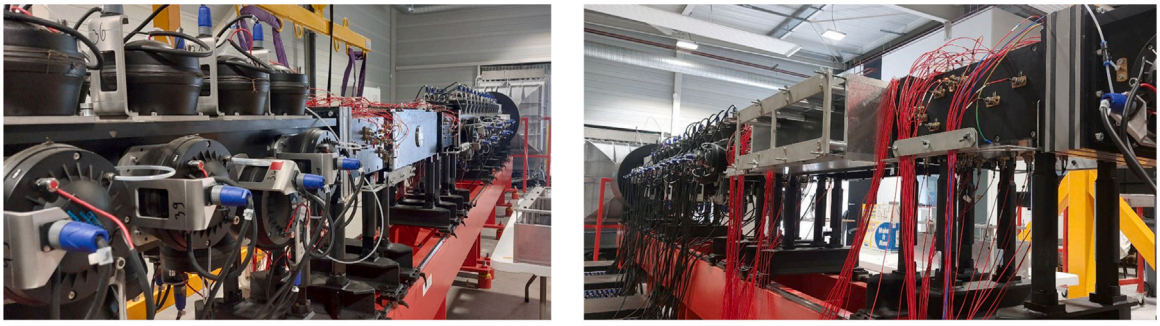

Fig. 4. Photos of the Maine Flow test rig, (a) hard-wall side view, (b) lined-wall side view. 60 microphones on each side of the test sample allow the decomposition of the incident and scattered acoustic fields. The modal content of the acoustic field is controlled by 90 acoustic sources located on each side of the test section. Between the two microphone sections, the 800 mm long test section has three rigid walls and one lined wall. The sample holder can be seen in (b). The measurement of the scattering matrix of a sample is made possible by imposing a number of independent acoustic fields incident from upstream and downstream.

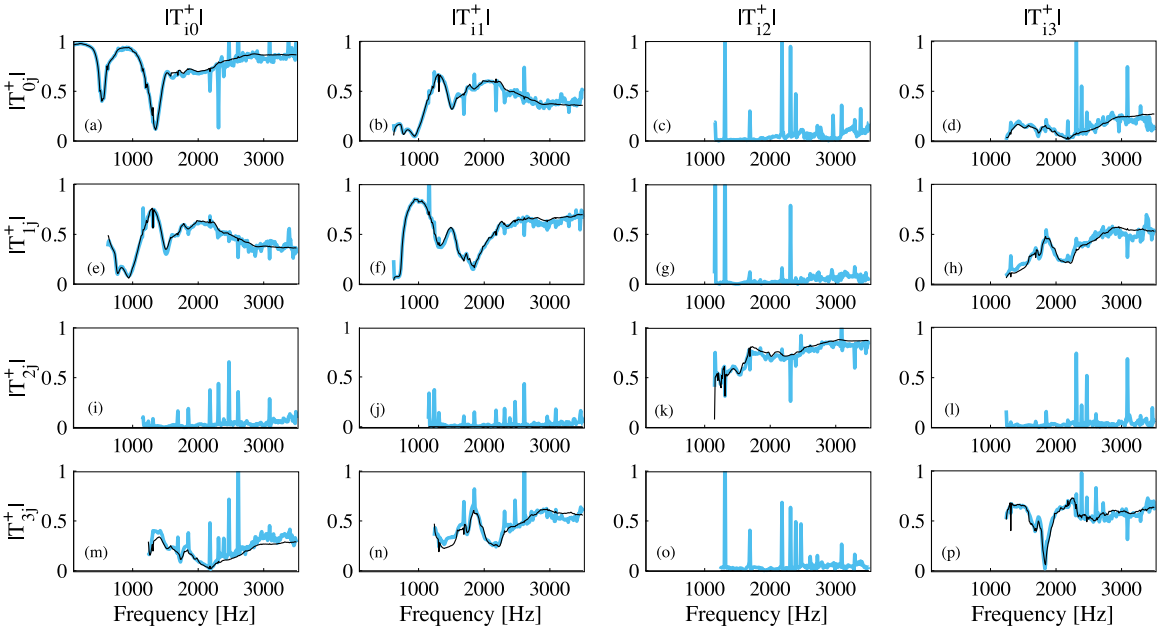

Fig. 5. Transmission matrix T^+ obtained for a double-degree of freedom liner at Mach 0. Each plot corresponds to a transmission coefficient associated with an incident mode (second subscript) and the mode that receives the energy (first subscript). Only the first four modes (including the plane wave, denoted 0) are shown here. Thus, the diagonal corresponds to the transmission of each mode to itself ((a) plane wave transmitted to itself), whereas extra-diagonal terms describe the energy transfers between the modes induced by the liner. Blue line: experimental results. Black Line: computed results using the impedance found in Section 4.3 with the full diagonal cost function Eq. (34). (For interpretation of the references to color in this figure legend, the reader is referred to the web version of this article.)

×150 mm, and the liner, which has a length of 800 mm, is mounted on the smallest side. The rig is equipped with 180 acoustic sources (90 on each side of the test section) that generate sweep-sine or broadband noise signals with incident wave amplitudes or overall sound pressure levels up to 150 dB between 300 Hz and 10 kHz. Finally, sixty microphones are mounted on each side of the sample to measure the acoustic field and to project it on the modes of the rigid duct. More details about this facility and the related experimental techniques can be found in [23–25].

3.2. Scattering matrix measurement

As in the numerical scattering problem defined by Eq. (24), the amplitudes of the waves scattered by the liner in the experiments are connected to the incident modes by the multimodal scattering matrix S. When N modes are cut-on in the rigid parts of the duct, S has dimensions $2N \times 2N$, and it can be identified using at least $2N$ independent excitation signals [24,26]. In practice, the

excitation cases are provided by sending a unit signal to each of the upstream and downstream source channels separately while assuming that the phases of the incident modes are random and not correlated together. As a result, each excitation case provides a new relation between incident and scattered waves. Combined together, these realizations form a linear system that is solved to get S [24]. This method is similar to the "two-source method" when only plane waves are present and does not rely on anechoic terminations upstream and downstream to be applicable.

The upstream transmission coefficients T^+ extracted from the measurement of S for a 3D printed Double Degree of Freedom (DDOF) liner are shown with blue curves in Fig. 5. For the sake of clarity, only the first four modes in terms of cut-on frequency are displayed, and the subscript 0 corresponds to the plane wave. Then, each plot corresponds to a transmission coefficient associated to an incident mode (second subscript) and the mode that receives the energy (first subscript). In other words, when considering the first column from top to bottom, it describes the transmission of the plane wave to itself, then to the first horizontal mode, then to the first vertical mode, and so on. In the same manner, the second column represents the transmission of the incident's first horizontal mode, and the third column concerns the incident's first vertical mode. Also, it can be noticed that the matrix diagonal corresponds to the transmission of each mode to itself, whereas the extra-diagonal terms describe the energy transfers between the modes due to the liner. The spotted spurious peaks correspond to cut-on frequencies, which induce a drop in the measurement precision. As expected for a DDOF, the coefficient $|T^+_{00}|$ displays two minima, which are also clearly visible on $|T^+_{11}|$. Only the second one appears in $|T^+_{33}|$ because of the cut-on frequency of this mode. Note also that since the second high-order mode is purely along the vertical direction and thus has only rigid wall boundary conditions, the liner effect is not observable with $|T^+_{22}|$, and there is no coupling between this mode and the other displayed ones.

From these experimental data, the inverse method that will be described hereafter is used to find an impedance that minimizes the difference between the numerical and the experimental diagonal transmission coefficients. The numerical transmission coefficients corresponding to the impedance obtained when the process stops are drawn in black in Fig. 5. The agreement with the experimental results is excellent, which means that the inverse method succeeds in converging towards an effective impedance that describes the liner effect well. It is finally noticed that the coefficients (for example T^+_{20}, T^+_{21} or T^+_{02}) that are theoretically zero because only one side is lined are effectively zero, whereas the experimental coefficients show noisy low values induced by measurements uncertainties.

3.3. Inverse method principle

The previous section explains the procedure for measuring the scattering matrix containing the transmission and reflection coefficients of a given liner sample, denoted $T^{\pm}_{e_{m,n}}$, $R^{\pm}_{e_{m,n}}$. On the other hand, Section 2.3 describes the numerical methods leading to the computed coefficients $T^{\pm}_{c_{m,n}}$, $R^{\pm}_{c_{m,n}}$ for a wall lined with a given impedance. These two paths are now brought together to form a cost function F, which is minimized when the impedance in the computation corresponds to the impedance of the studied sample:

$$F = \sum_{m,n=0}^{M} w_{T^+_{m,n}} |T^+_{e_{m,n}} - T^+_{c_{m,n}}| + \sum_{m,n=0}^{M} w_{T^-_{m,n}} |T^-_{e_{m,n}} - T^-_{c_{m,n}}| + \sum_{m,n=0}^{M} w_{R^+_{m,n}} |R^+_{e_{m,n}} - R^+_{c_{m,n}}| + \sum_{m,n=0}^{M} w_{R^-_{m,n}} |R^-_{e_{m,n}} - R^-_{c_{m,n}}|. \tag{33}$$

The total number of modes M taken into account in the cost function depends on the number of propagating modes at the considered frequency. The weights w_{T^+}, w_{T^-}, w_{R^+}, w_{R^-} permit giving more importance to some of the transmission coefficients or to one direction of propagation if needed. In the present paper, the cost function is only based on the transmission coefficients ($w_{R^\pm} = 0$) since the reflection coefficients have very low magnitudes. Furthermore, the largest terms of the transmission matrix are the diagonal ones. Thus, in the rest of this study, only these diagonal coefficients are taken into account, with a common weight equal to one ($w_{T^+_{m,n}} = \delta_{mn}$ for streamwise propagation and $w_{T^-_{m,n}} = \delta_{mn}$ for upstream propagation, using Kronecker delta notation). With these assumptions, and separating in upstream propagation and streamwise propagation cost functions, Eq. (33) is written:

$$F^{\pm}_{diag} = \sum_{m=0}^{M} |T^{\pm}_{e_{m,m}} - T^{\pm}_{c_{m,m}}|. \tag{34}$$

The $\pm$ superscript indicates if the acoustic sources are upstream (+) or downstream (−) of the test section. In a few cases, the cost function based on only one mode will be used, and the summation will be omitted in Eq. (34).

In this study, two methods are used to minimize the cost function Eq. (34): a local optimization algorithm and a global one. The first one uses the *fminsearch* MATLAB function, which performs local optimization based on the Nelder–Mead simplex direct search algorithm. In this framework, an initial guess for the liner impedance is needed. It enables a first computation of the scattering matrix through the multimodal method before the minimization process converges to the correct impedance. To obtain this initial impedance function, the liner concepts evaluated in MAINE Flow are also characterized in a smaller test rig with a 50×40 mm^2 cross-section where only plane wave propagates [27,28]. The lined surface is 200×50 mm^2, and the measurements are performed using a sine-sweep going from 100 to 3500 Hz with a step of 5 Hz. The impedance is computed using an inverse method based on a 2D computation of the acoustic field [7]. This initial guess based on the measurement of the same liner concept ensures a relatively rapid convergence of the minimization process and reduces the likelihood of encountering incorrect local minima in the cost function. Note that an impedance computed by a numerical or an analytical model can also be used as a starting point.

However, this method is sensible to the choice of the initial guess, and having the latter is not always possible. Thus, a global optimization process is also implemented. We have selected Particle Swarm Optimization (PSO) for its straightforward

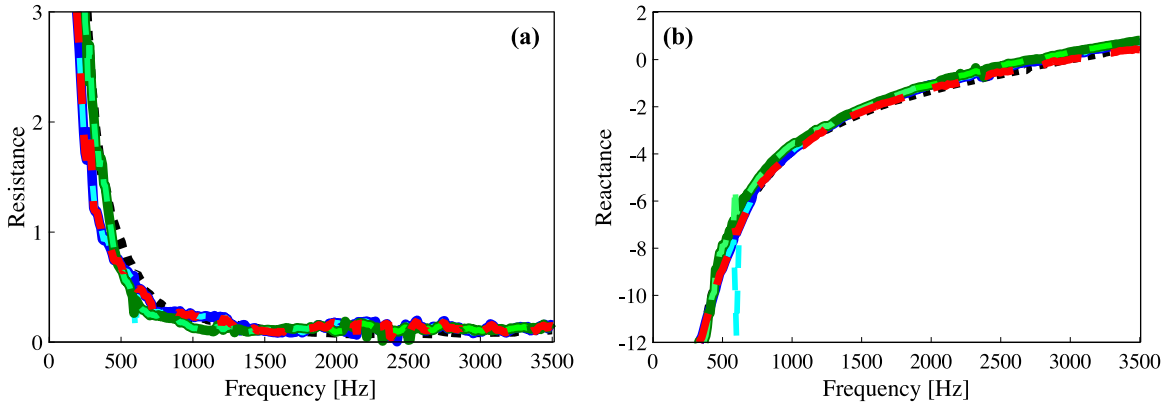

Fig. 6. SDOF educed resistance (a) and reactance (b) using the full diagonal cost function Eq. (34). The two color classes correspond to acoustic sources located upstream (blue) and downstream (green) of the test section. Dark solid lines: local optimization results with the small test duct impedance (black dashed line) as an initial guess. Light dashed lines: results with the global optimization. All these curves are based on acoustic computations using 10×10 modes except the red curve based on a 30×30 computation with upstream source and local optimization process. (For interpretation of the references to color in this figure legend, the reader is referred to the web version of this article.)

implementation and its robust performance across both discrete and continuous search domains [29]. The process starts with creating initial particles, each assigned an initial velocity. The cost function is then evaluated at each particle's position to find the minimum function value and its location. New velocities are calculated based on the current velocities, each particle's best-known position, and the best positions of neighboring particles. This iterative process updates particle positions, recalculating them as the sum of the previous position and velocity, with adjustments to ensure particles stay within defined boundaries. The iterations continue until a predefined stopping criterion is met. For the present study, the search field is bounded between 0.01 and 20 for the non-dimensional liner resistance and between -40 and 10 for the non-dimensional liner reactance across the frequency range of interest. For each frequency, 20 particles with random initial values are used as the population. The maximum of allowed iterations is 500, and the termination tolerance on the function value is 10^{-6}. However, it is important to acknowledge that the primary drawback of this algorithm lies in its computational time. Hence, a proposed solution is to employ first PSO with coarse steps, then followed by the local optimization routine which is relatively fast and accurate when starting close to the correct solution.

4. Results without flow

In this section, the impedance eduction results are shown in the absence of flow. First, a Single Degree of Freedom (SDOF) liner is considered to compare the MAINE Flow results with the initial guess obtained in a smaller facility. The performance of the local and global algorithms are also compared, and the effect of the number of modes M chosen for the cost function Eq. (34) is studied. Finally, the very satisfactory results are confirmed through the study of a Double Degrees of Freedom (DDOF) liner.

4.1. Performance of the local and global optimization

The tests are conducted on an SDOF 3D printed by stereolithography, with a perforated top layer, rectangular cavities, and a rigid backing. Fig. 6 displays the resistance and reactance found to minimize the cost function Eq. (34) for the SDOF liner. A perfect matching between the local (dark solid lines) and global (light dashed lines) optimizations shows that both methods converge to the same impedance. Thus, PSO is a useful tool when the initial guess is not available or if the local process seems stuck on a wrong local minimum. In practice, convergence to an incorrect local minimum is suspected when the obtained impedance at a specific frequency or frequency range deviates from the values observed at neighboring frequencies. Furthermore, an incorrect minimum is likely identified if the impedance does not match an expected impedance model (for standard liners) or measurements of the same liner in a different facility. In the present study, local and global results are also found to be in very good agreement with the impedance obtained in the small duct and displayed in black dashed lines. This fact validates both the manufacturing process of the samples and the proposed eduction method. Moreover, the results for waves generated upstream or downstream of the test section are close because of the reciprocity principle. However, a small discrepancy between the downstream and upstream propagation remains and can be explained by factors such as microphone calibration errors, measurement uncertainties, and possible slow flow ($M_a < 0.02$) that can occur in this large facility when the fan is off. Finally, note that all these impedances are based on acoustic computations using 10×10 modes except the red curve based on a 30×30 modes computation with upstream source and local optimization process. Since both results are equal, it is possible to take fewer modes into account in order to earn computational time while maintaining great eduction performance. Thus, 10×10 modes are used in the remainder of the paper.

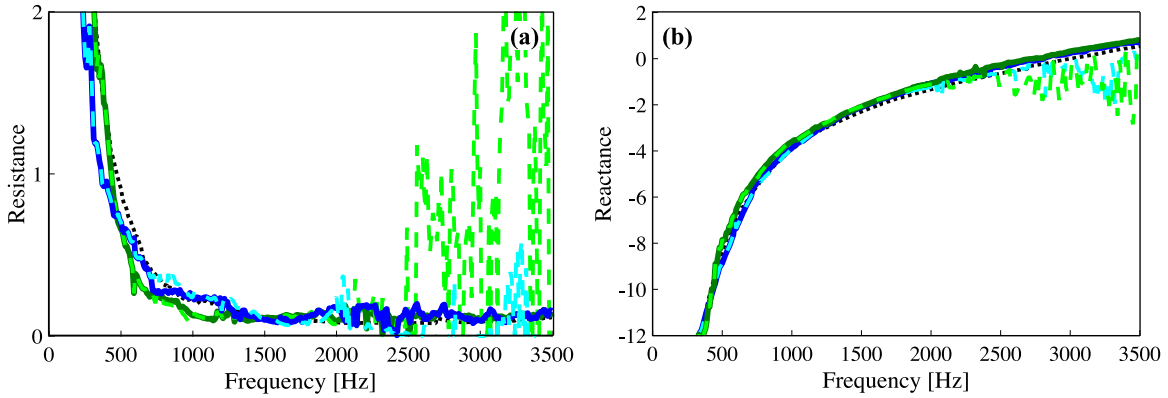

Fig. 7. SDOF educed resistance (a) and reactance (b) using the local optimization process. The two color classes correspond to acoustic sources located upstream (blue) and downstream (green) of the test section. Dark solid lines: the cost function uses all the diagonal coefficients of the transmission matrix as stated by Eq. (34). Light dashed lines: the cost function is only based on the transmission of the plane wave to itself $F^{\pm} = |T^{\pm}_{e_{0,0}} - T^{\pm}_{c_{0,0}}|$. Black dashed line: the initial guess obtained in the small-scale facility. (For interpretation of the references to color in this figure legend, the reader is referred to the web version of this article.)

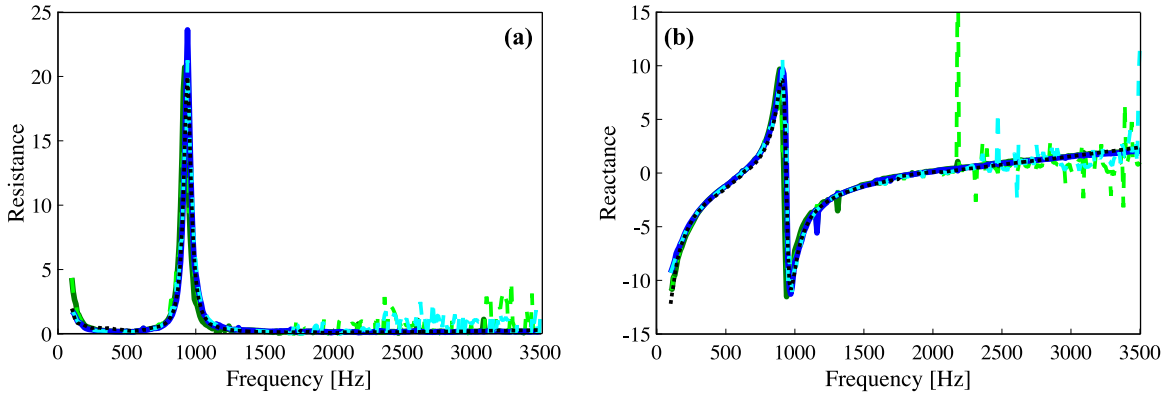

Fig. 8. DDOF educed resistance (a) and reactance (b) using the local optimization process. The two color classes correspond to acoustic sources located upstream (blue) and downstream (green) of the test section. Dark solid lines: the cost function uses all the diagonal coefficients of the transmission matrix. Light dashed lines: the cost function is only based on the transmission of the plane wave to itself. Black dashed line: The initial guess obtained in the small-scale facility. (For interpretation of the references to color in this figure legend, the reader is referred to the web version of this article.)

4.2. Effect of the cost function

In order to evaluate the effect of the number of modes M in the cost function Eq. (34), we compare the process of considering all the cut-on modes at a given frequency against taking only into account the transmission of the plane wave to itself. Note that at 3500 Hz, the highest studied frequency, 19 modes are cut-on. Fig. 7 displays the educed impedance in the absence of flow for these two cost functions, and the results agree well up to 2000 Hz. Above this range, the educed resistance and reactance are noisy and deviate from the other results when considering only the first coefficient in the transmission matrix. This is visible for both acoustic source locations and should be explained by the fact that, in this high-frequency range, the plane wave is weakly attenuated, and many impedances correspond to such a large acoustic transmission. Thus, the eduction process fails, and the plane wave is insufficient in this multi-modal context. Nevertheless, the great results achieved using the full cost function Eq. (34) show the capability of the developed inverse method to tackle this challenge.

4.3. Double degree of freedom liner

The SDOF sample permits the validation of the proposed impedance eduction method by providing results that agree with the characterization of the same liner in a much smaller duct under plane wave excitation. This experiment also highlights the benefits of using the multi-modal transmission matrix at high frequencies.

As a second example, a DDOF liner 3D printed by stereolithography with a perforated top layer, rectangular cavities, a septum, and a rigid backing is evaluated. Fig. 8 compares again the impedance obtained if the full cost function Eq. (34) is used or if only the plane-wave coefficient is kept. This is done in the absence of flow for acoustic sources either located upstream or downstream of the test section. Before 2000 Hz, all the curves fit together, and the impedance agrees very well with the impedance educed for

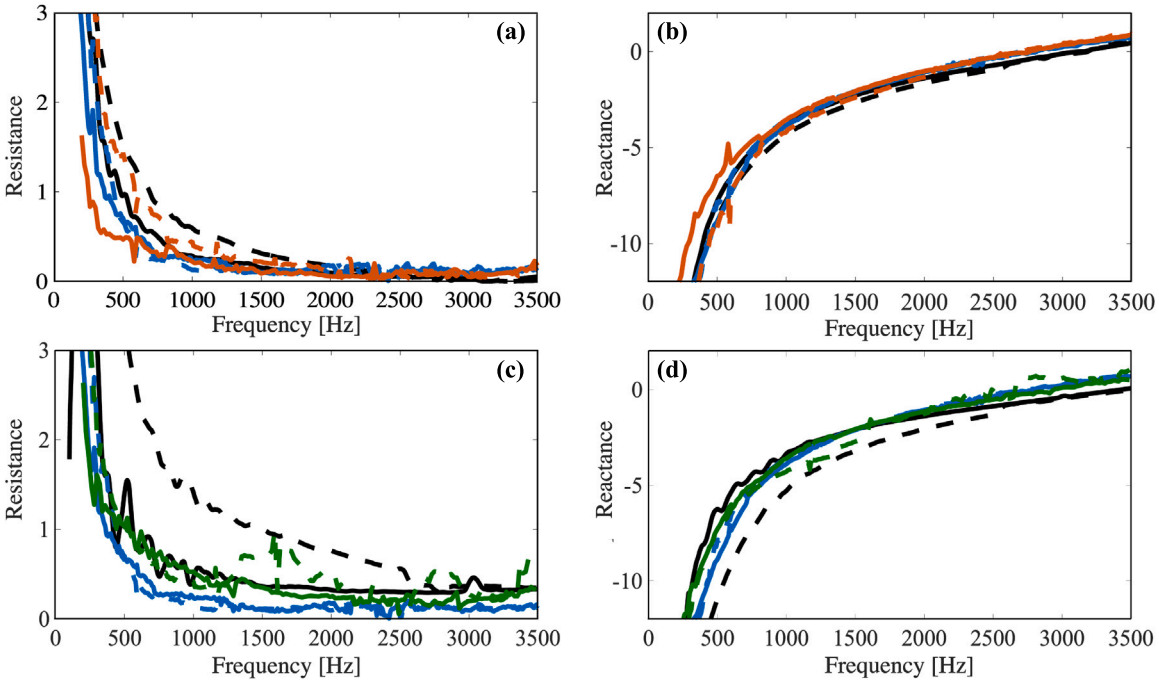

Fig. 9. SDOF educed resistance (a, c) and reactance (b, d) using the global optimization process with the full diagonal cost function. The two line classes correspond to acoustic sources located upstream (solid) and downstream (dashed) of the test section. Blue: educed impedance without flow, $M_a = 0$. (a, b) MAINE Flow (red) and small-scale facility (black) results at $M_a = 0.1$. (c, d) MAINE Flow (green) and small-scale facility (black) results at $M_a = 0.2$. (For interpretation of the references to color in this figure legend, the reader is referred to the web version of this article.)

the same liner concept in the small test bench. However, at higher frequencies, it is necessary to take into account the higher-order modes to avoid spurious peaks and noisy data. Indeed, considering only the plane wave shows poor accuracy or even complete failure in convergence.

Finally, the impedance found for upstream sources using the full diagonal of the transmission matrix into the cost function is used to compute, thanks to the 3D multimodal method, the transmission matrix of the sample. The latter is compared to the measured one in Fig. 5. It can be seen that the local optimization process leads to a result that fits really well with the measured coefficients in all the cases shown here and for the whole considered frequency range.

5. Results with flow

In the previous section, the study of two liners validated the proposed inverse eduction process in the absence of flow. Here, the effects of a low Mach number flow (up to $M_a = 0.2$) on the acoustic properties of the SDOF sample are evaluated. To achieve this, the cost function Eq. (34), which has demonstrated high accuracy at high frequencies, is minimized using a global optimization algorithm. This global approach is preferred over a local one to avoid the occurrence of local minima.

Fig. 9 compares, against the no-flow results, the educed resistance and reactance for waves propagating both with and against the flow, at $M_a = 0.1$ (top) and $M_a = 0.2$ (bottom). At $M_a = 0.1$, the impedance remains close to the no-flow measurements, suggesting weak flow effects. However, it can be noticed that the discrepancies between impedance measured for waves propagating with or against the flow increase. In particular, the resistance seen by waves propagating upstream is larger than the one seen by waves propagating downstream in the low and mid-frequency bands. In the high-frequency band, both resistances converge towards the same values as the no-flow case. The discrepancies between both propagation directions are also visible on the educed reactance. As for the no-flow case, the results obtained in the small duct facility for the same liner are also displayed. On most of the frequency bands, the results obtained for an upstream acoustic source are similar in the two facilities, and the discrepancies at low frequencies could be attributed to uncertainties in the presence of weak attenuation. However, it can also be seen that for downstream acoustic sources, the educed resistance is larger in the small duct facility, while the reactance is smaller.

Fig. 9 (bottom) shows that the effects of flow are more significant at $M_a = 0.2$. In particular, the resistances in MAINE flow are higher than those obtained without flow across the entire frequency range. Again, the resistance for waves propagating against the flow is larger. Although the results for the upstream acoustic source align reasonably well with typical SDOF behavior, the impedance for acoustic sources downstream of the test section shows oscillations in the mid-frequency band and spurious values at the cut-on frequency of the higher-order modes. It is important to note that, as shown in [18], for waves propagating against the flow at $M_a \geq 0.2$, shear flow effects cannot be neglected. Therefore, the results presented should be considered with caution

and provide only a rough estimate of the effects of flow on the impedance. Including shear flow effects will be the next step in our research. This will require using the Linearized Euler Equations or Pridmore-Brown Equation instead of the Convected Helmholtz equation.

Compared with the small-duct facility, what is observed for $M_a = 0.1$ is much more visible at $M_a = 0.2$: the impedances obtained for the upstream acoustic sources agree well between the two facilities, whereas the results for the downstream acoustic sources are much more different in the small duct. The present paper does not claim to provide definitive explanations for these different behaviors observed in the two test rigs. However, we propose two hypotheses that may help guide future investigations:

- The boundary layer and flow profile are likely to differ significantly between the two ducts, leading to different scale relationships between the boundary layer and the wavelength. This could affect the sound-flow interaction and, consequently, the effective impedance.
- As noted in the paper, recent studies have shown that shear flow, which is neglected in this study, has a more pronounced influence on upstream wave propagation. This omission may lead to uncertainties in the MAINE Flow measurement framework, potentially causing an underestimation of the liner resistance.

However, despite the complex multi-modal framework imposed by the MAINE Flow facility, the presented method already demonstrates great performance. To our knowledge, the robustness of the impedance eduction shown here in the absence of flow has never been achieved in the existing literature.

6. Conclusion

This paper introduces a 3D multimodal method capable of educing the impedance in large ducts where the multi-modal acoustic field is present. It is based on a multimodal computation of the scattering matrix and the experimental characterization of the sample in the MAINE Flow facility. The method is validated in the absence of the flow by comparing the educed impedance with the obtained impedance from the same sample in a small test bench. To question the validity of the method with simple and complex samples, the evaluation is done for both SDOF and DDOF cases, indicating that its satisfactory performance is not limited to simple cases. It has also been confirmed that the robustness and accuracy of the method are significantly improved by taking into account more coefficients in the cost function, which is done by comparing the results obtained with a cost function based only on the plane wave and a cost function based on all the available diagonal coefficients of the transmission matrices. The gain in robustness is, in particular, important at high frequencies, where many modes propagate. This suggests that impedance eduction in large ducts should be performed with such methods based on the scattering matrix since the multimodal nature of the latter fits the constraints of the acoustic field and thus does not fail in terms of performance when frequency increases.

In parallel, a global optimization process is introduced and validated, making the method suitable for cases where the studied sample is unknown. Regarding the outstanding results obtained in no-flow conditions, the presented inverse method is evaluated in the presence of flow for a SDOF sample. At Mach 0.1, the impedance is clearly obtained for the whole frequency band for both upstream and downstream configurations. At Mach 0.2, the results obtained when waves propagate against the flow include spurious values and unexpected oscillations, whereas they remain consistent when waves propagate with the flow. However, it is known that the shear flow effects, which are neglected here, are more important against the flow and are significant at Mach 0.2. This will be the major point to be evaluated for the next step studies so that the present method can be used at higher flow speeds and for the two wave propagation directions.

CRediT authorship contribution statement

Hamid Rashidi: Writing – review & editing, Writing – original draft, Visualization, Validation, Software, Methodology, Investigation, Formal analysis, Conceptualization. **Joachim Golliard:** Writing – review & editing, Supervision, Investigation, Conceptualization. **Thomas Humbert:** Writing – review & editing, Supervision, Investigation, Formal analysis, Conceptualization.

Declaration of competing interest

The authors declare the following financial interests/personal relationships which may be considered as potential competing interests: Hamid Rashidi, Joachim Golliard, Thomas Humbert reports financial support was provided by French Civil Aviation Agency (DGAC). If there are other authors, they declare that they have no known competing financial interests or personal relationships that could have appeared to influence the work reported in this paper.

Acknowledgments

This work was carried out in the framework of the MAMBO project, supported by the French Civil Aviation Agency (DGAC) under DGAC Convention 2021–50, the “France Relance” national recovery plan, and the “Next Generation EU” European recovery plan.

Appendix A. Complementary computation needed to express the continuity conditions at interfaces in matrix form

We recall here Eq. (22) which expresses the continuity conditions at the upstream liner interface:

$$\begin{pmatrix} I & I \\ -\mathrm{j}K_{mn}^{+}\Omega+\Gamma_2 & -\mathrm{j}K_{mn}^{-}\Omega+\Gamma_2 \end{pmatrix}\begin{pmatrix}\mathbf{A_1}\\ \mathbf{B_1}\end{pmatrix} = \begin{pmatrix} \Gamma_1 X^{+} & \Gamma_1 X^{-}E_L^{-} \\ X^{+}(-\mathrm{j}\Gamma_1 K_Y^{+}\Omega+\Gamma_3) & X^{-}E_L^{-}(-\mathrm{j}\Gamma_1 K_Y^{-}\Omega+\Gamma_3) \end{pmatrix}\begin{pmatrix}\mathbf{A_2}\\ \mathbf{B_3}\end{pmatrix}. \tag{A.1}$$

Then, on the road towards the scattering matrix, our goal is to express simply this relation as:

$$\begin{pmatrix}\mathbf{A_1}\\ \mathbf{B_1}\end{pmatrix} = \begin{pmatrix} x_1 & x_2 \\ x_3 & x_4 \end{pmatrix}\begin{pmatrix}\mathbf{A_2}\\ \mathbf{B_3}\end{pmatrix}. \tag{A.2}$$

The expressions for x_1, x_2, x_3, and x_4 are not given in the core of the paper, for the sake of brevity. Their computations and expressions are detailed thus below.

Indeed, if Eq. (22) is seen as a general system of the form

$$\begin{pmatrix} a & b \\ c & d \end{pmatrix}\begin{pmatrix}\mathbf{A_1}\\ \mathbf{B_1}\end{pmatrix} = \begin{pmatrix} e & f \\ g & h \end{pmatrix}\begin{pmatrix}\mathbf{A_2}\\ \mathbf{B_3}\end{pmatrix}, \tag{A.3}$$

we can write:

$$\begin{aligned}\begin{pmatrix}\mathbf{A_1}\\ \mathbf{B_1}\end{pmatrix} &= \frac{1}{ad-bc}\begin{pmatrix} d & -b \\ -c & a \end{pmatrix}\begin{pmatrix} e & f \\ g & h \end{pmatrix}\begin{pmatrix}\mathbf{A_2}\\ \mathbf{B_3}\end{pmatrix} \\ &= \frac{1}{ad-bc}\begin{pmatrix} de-bg & df-bh \\ -ce+ag & -cf+ah \end{pmatrix}\begin{pmatrix}\mathbf{A_2}\\ \mathbf{B_3}\end{pmatrix},\end{aligned}$$

with

$$\begin{aligned} a &= I, \quad b = I, \quad c = -\mathrm{j}K_{mn}^{+}\Omega+\Gamma_2 \quad d = -\mathrm{j}K_{mn}^{-}\Omega+\Gamma_2, \quad e = \Gamma_1 X^{+} \\ f &= \Gamma_1 X^{-}E_L^{-}, \quad g = X^{+}(-\mathrm{j}\Gamma_1 K_Y^{+}\Omega+\Gamma_3), \quad h = X^{-}E_L^{-}(-\mathrm{j}\Gamma_1 K_Y^{-}\Omega+\Gamma_3). \end{aligned}$$

Thus,

$$x_1 = \frac{de-bg}{ad-bc} = \frac{X^{+}(\Gamma_1(\Gamma_2+\mathrm{j}\Omega(K_Y^{+}-K_{mn}^{-}))-\Gamma_3)}{\mathrm{j}\Omega(K_{mn}^{+}-K_{mn}^{-})}, \tag{A.4}$$

$$x_2 = \frac{df-bh}{ad-bc} = \frac{X^{-}E_L^{-}(\Gamma_1(\Gamma_2+\mathrm{j}\Omega(K_Y^{-}-K_{mn}^{-}))-\Gamma_3)}{\mathrm{j}\Omega(K_{mn}^{+}-K_{mn}^{-})}, \tag{A.5}$$

$$x_3 = \frac{-ce+ag}{ad-bc} = \frac{X^{+}(\Gamma_1(\mathrm{j}\Omega(K_{mn}^{+}-K_Y^{+})-\Gamma_2)+\Gamma_3)}{\mathrm{j}\Omega(K_{mn}^{+}-K_{mn}^{-})}, \tag{A.6}$$

$$x_4 = \frac{-cf+ah}{ad-bc} = \frac{X^{-}E_L^{-}(\Gamma_1(\mathrm{j}\Omega(K_{mn}^{+}-K_Y^{-})-\Gamma_2+)+\Gamma_3)}{\mathrm{j}\Omega(K_{mn}^{+}-K_{mn}^{-})}. \tag{A.7}$$

For the downstream interface, let us first recall Eq. (23):

$$\begin{pmatrix} I & I \\ -\mathrm{j}K_{mn}^{+}\Omega+\Gamma_2 & -\mathrm{j}K_{mn}^{-}\Omega+\Gamma_2 \end{pmatrix}\begin{pmatrix}\mathbf{A_4}\\ \mathbf{B_4}\end{pmatrix} = \begin{pmatrix} \Gamma_1 X^{+}E_L^{+} & \Gamma_1 X^{-} \\ X^{+}E_L^{+}(\Gamma_3-\mathrm{j}\Gamma_1 K_Y^{+}\Omega) & X^{-}(\Gamma_3-\mathrm{j}\Gamma_1 K_Y^{-}\Omega) \end{pmatrix}\begin{pmatrix}\mathbf{A_2}\\ \mathbf{B_3}\end{pmatrix}. \tag{A.8}$$

Again, this system can be written under the form

$$\begin{pmatrix}\mathbf{A_4}\\ \mathbf{B_4}\end{pmatrix} = \begin{pmatrix} y_1 & y_2 \\ y_3 & y_4 \end{pmatrix}\begin{pmatrix}\mathbf{A_2}\\ \mathbf{B_3}\end{pmatrix} = \frac{1}{ad-bc}\begin{pmatrix} de-bg & df-bh \\ -ce+ag & -cf+ah \end{pmatrix}\begin{pmatrix}\mathbf{A_2}\\ \mathbf{B_3}\end{pmatrix}, \tag{A.9}$$

but with this time:

$$\begin{aligned} a &= I, \quad b = I, \quad c = -\mathrm{j}K_{mn}^{+}\Omega+\Gamma_2 \quad d = -\mathrm{j}K_{mn}^{-}\Omega+\Gamma_2, \quad e = \Gamma_1 X^{+}E_L^{+} \\ f &= \Gamma_1 X^{-}, \quad g = X^{+}E_L^{+}(-\mathrm{j}\Gamma_1 K_Y^{+}\Omega+\Gamma_3), \quad h = X^{-}(-\mathrm{j}\Gamma_1 K_Y^{-}\Omega+\Gamma_3). \end{aligned}$$

It yields:

$$y_1 = \frac{de-bg}{ad-bc} = \frac{X^{+}E_L^{+}(\Gamma_1(\Gamma_2+\mathrm{j}\Omega(K_Y^{+}-K_{mn}^{-}))-\Gamma_3)}{\mathrm{j}\Omega(K_{mn}^{+}-K_{mn}^{-})}, \tag{A.10}$$

$$y_2 = \frac{df-bh}{ad-bc} = \frac{X^{-}(\Gamma_1(\Gamma_2+\mathrm{j}\Omega(K_Y^{-}-K_{mn}^{-}))-\Gamma_3)}{\mathrm{j}\Omega(K_{mn}^{+}-K_{mn}^{-})}, \tag{A.11}$$

$$y_3 = \frac{-ce+ag}{ad-bc} = \frac{X^{+}E_L^{+}(\Gamma_1(\mathrm{j}\Omega(K_{mn}^{+}-K_Y^{+})-\Gamma_2)+\Gamma_3)}{\mathrm{j}\Omega(K_{mn}^{+}-K_{mn}^{-})}, \tag{A.12}$$

$$y_4 = \frac{-cf + ah}{ad - bc} = \frac{X^-(\Gamma_1(\mathrm{j}\Omega(K_{mn}^+ - K_Y^-) - \Gamma_2 +) + \Gamma_3)}{\mathrm{j}\Omega(K_{mn}^+ - K_{mn}^-)}. \tag{A.13}$$

Appendix B. From the transfer matrix to the scattering matrix

Here, we provide the details about the computations that permit going from the transfer matrix formulation given by Eq. (29),

$$\begin{pmatrix} \mathbf{A_1} \\ \mathbf{B_1} \end{pmatrix} = \frac{1}{y_1y_4 - y_2y_3} \begin{pmatrix} x_1y_4 - x_2y_3 & -x_1y_2 + x_2y_1 \\ x_3y_4 - x_4y_3 & -x_3y_2 + x_4y_1 \end{pmatrix} \begin{pmatrix} \mathbf{A_4} \\ \mathbf{B_4} \end{pmatrix}, \tag{B.1}$$

to the scattering matrix formulation given by Eq. (24),

$$\begin{pmatrix} \mathbf{A_4} \\ \mathbf{B_1} \end{pmatrix} = \begin{pmatrix} T^+ & R^- \\ R^+ & T^- \end{pmatrix} \begin{pmatrix} \mathbf{A_1} \\ \mathbf{B_4} \end{pmatrix}. \tag{B.2}$$

We write the first system under the form:

$$\begin{pmatrix} \mathbf{A_1} \\ \mathbf{B_1} \end{pmatrix} = \begin{pmatrix} a & b \\ c & d \end{pmatrix} \begin{pmatrix} \mathbf{A_4} \\ \mathbf{B_4} \end{pmatrix}, \tag{B.3}$$

with

$$a = \frac{x_1y_4 - x_2y_3}{y_1y_4 - y_2y_3}, \qquad b = \frac{-x_1y_2 + x_2y_1}{y_1y_4 - y_2y_3},$$
$$c = \frac{x_3y_4 - x_4y_3}{y_1y_4 - y_2y_3}, \qquad d = \frac{-x_3y_2 + x_4y_1}{y_1y_4 - y_2y_3}.$$

It can then be noticed that $\mathbf{A_4} = \frac{1}{a}\mathbf{A_1} - ba\mathbf{B_4}$ and $\mathbf{B_1} = \frac{c}{a}\mathbf{A_1} - \frac{1}{a}(da - cb)\mathbf{B_4}$. Thus, we have :

$$T^+ = \frac{1}{a}, \qquad R^- = -\frac{b}{a}, \qquad R^+ = \frac{c}{a}, \qquad T^- = \frac{1}{a}(da - cb).$$

It is easy to get then:

$$T^+ = \frac{y_1 - \frac{y_2y_3}{y_4}}{x_1 - \frac{x_2y_3}{y_4}}, \qquad R^+ = \frac{x_3 - \frac{x_4y_3}{y_4}}{x_1 - \frac{x_2y_3}{y_4}}, \qquad R^- = \frac{y_2 - \frac{y_1x_2}{x_1}}{y_4 - \frac{y_3x_2}{x_1}}. \tag{B.4}$$

The last scattering coefficient, T^-, can be put in a compact form, but this requires simplifying :

$$\frac{(x_1y_4 - x_2y_3)(-x_3y_2 + x_4y_1) - (x_3y_4 - x_4y_3)(-x_1y_2 + x_2y_1)}{(x_1y_4 - x_2y_3)(y_1y_4 - y_2y_3)}. \tag{B.5}$$

Expanding the first term of the numerator leads to:

$$(x_1y_4 - x_2y_3)(-x_3y_2 + x_4y_1) = -x_1x_3y_4y_2 + x_1x_4y_4y_1 + x_2x_3y_3y_2 - x_2x_4y_3y_1,$$

while the second one reads:

$$(x_3y_4 - x_4y_3)(-x_1y_2 + x_2y_1) = -x_1x_3y_4y_2 + x_2x_3y_4y_1 + x_1x_4y_3y_2 - x_2x_4y_3y_1.$$

Subtracting these two expressions yields, after simplifications, to:

$$x_1x_4y_4y_1 + x_2x_3y_3y_2 - x_2x_3y_4y_1 - x_1x_4y_3y_2 = (y_4y_1 - y_3y_2)(x_1x_4 - x_2x_3).$$

Then, it allows the simplification of T^- as

$$T^- = \frac{(y_4y_1 - y_3y_2)(x_1x_4 - x_2x_3)}{(x_1y_4 - x_2y_3)(y_1y_4 - y_2y_3)} = \frac{x_1x_4 - x_2x_3}{x_1y_4 - x_2y_3} = \frac{x_4 - \frac{x_3x_2}{x_1}}{y_4 - \frac{y_3x_2}{x_1}}. \tag{B.6}$$

Data availability

Data will be made available on request.

References

[1] X. Ma, Z. Su, Development of acoustic liner in aero engine: a review, Sci. China Technol. Sci. 63 (2020) 2491–2504, http://dx.doi.org/10.1007/s11431-019-1501-3.

[2] D.L. Sutliff, D.M. Nark, M.G. Jones, Multi-degree-of-freedom liner development: Concept to flight test, Int. J. Aeroacoustics 20 (5–7) (2021) 792–825, http://dx.doi.org/10.1177/1475472X211023860.

[3] C. Weng, A. Schulz, D. Ronneberger, L. Enghardt, F. Bake, Flow and viscous effects on impedance eduction, AIAA J. 56 (3) (2018) 1118–1132, http://dx.doi.org/10.2514/1.J055838.

[4] R. Troian, D. Dragna, C. Bailly, M.-A. Galland, Broadband eduction of liner impedance under multimodal acoustic propagation, in: 22nd AIAA/CEAS Aeroacoustics Conference, 2016, p. 2725, http://dx.doi.org/10.2514/6.2016-2725.

[5] A.M. Spillere, L.A. Bonomo, J.A. Cordioli, E.J. Brambley, Testing impedance eduction boundary conditions with four wavenumbers per frequency, in: 25th AIAA/CEAS Aeroacoustics Conference, 2019, p. 2488, http://dx.doi.org/10.2514/6.2019-2488.
[6] R. Roncen, E. Piot, F. Méry, F. Simon, M.G. Jones, D.M. Nark, Wavenumber-based impedance eduction with a shear grazing flow, AIAA J. 58 (7) (2020) 3040–3050, http://dx.doi.org/10.2514/1.J059100.
[7] Y. Aurégan, M. Leroux, V. Pagneux, Measurement of liner impedance with flow by an inverse method, in: 10th AIAA/CEAS Aeroacoustics Conference, 2004, p. 2838, http://dx.doi.org/10.2514/6.2004-2838.
[8] W.R. Watson, M.G. Jones, A comparative study of four impedance eduction methodologies using several test liners, in: 19th AIAA/CEAS Aeroacoustics Conference, 2013, p. 2274, http://dx.doi.org/10.2514/6.2013-2274.
[9] R. Kumaresan, D. Tufts, Estimating the parameters of exponentially damped sinusoids and pole-zero modeling in noise, IEEE Trans. Acoust. Speech Signal Process. 30 (6) (1982) 833–840, http://dx.doi.org/10.1109/TASSP.1982.1163974.
[10] Q. Xianghai, X. Bo, W. Long, M. Yang, J. Xiaodong, Investigation of straightforward impedance eduction method on single-degree-of-freedom acoustic liners, Chin. J. Aeronaut. 31 (12) (2018) 2221–2233, http://dx.doi.org/10.1016/j.cja.2018.08.014.
[11] X. Jing, S. Peng, X. Sun, A straightforward method for wall impedance eduction in a flow duct, J. Acoust. Soc. Am. 124 (1) (2008) 227–234, http://dx.doi.org/10.1121/1.2932256.
[12] W.R. Watson, M.G. Jones, J.C. June, Single mode theory for impedance eduction in large-scale ducts with grazing flow, in: 20th AIAA/CEAS Aeroacoustics Conference, 2014, p. 3351, http://dx.doi.org/10.2514/6.2014-3351.
[13] L.A. Bonomo, A.M. Spillere, J.A. Cordioli, Parametric uncertainty analysis for impedance eduction based on Prony's method, AIAA J. 58 (8) (2020) 3625–3638, http://dx.doi.org/10.2514/1.J059071.
[14] U. Ingard, Influence of fluid motion past a plane boundary on sound reflection, absorption, and transmission, J. Acoust. Soc. Am. 31 (7) (1959) 1035–1036, http://dx.doi.org/10.1121/1.1907805.
[15] M. Myers, On the acoustic boundary condition in the presence of flow, J. Sound Vib. 71 (3) (1980) 429–434, http://dx.doi.org/10.1016/0022-460X(80)90424-1.
[16] W.R. Watson, M.H. Carpenter, M.G. Jones, Performance of Kumaresan and Tufts algorithm in liner impedance eduction with flow, AIAA J. 53 (4) (2015) 1091–1102, http://dx.doi.org/10.2514/1.J053705.
[17] X. Jing, S. Peng, L. Wang, X. Sun, Investigation of straightforward impedance eduction in the presence of shear flow, J. Sound Vib. 335 (2015) 89–104, http://dx.doi.org/10.1016/j.jsv.2014.08.031.
[18] J. Yang, T. Humbert, J. Golliard, G. Gabard, Shear flow effects in a 2D duct: Influence on wave propagation and direct impedance eduction, J. Sound Vib. 576 (2024) 118296, http://dx.doi.org/10.1016/j.jsv.2024.118296.
[19] L. Chen, L. Du, X. Wang, X. Jing, X. Sun, A three-dimensional straightforward method for liner impedance eduction in uniform grazing flow, J. Sound Vib. 468 (2020) 115119, http://dx.doi.org/10.1016/j.jsv.2019.115119.
[20] X. Qiu, J. Yang, X. Jing, L. Du, X. Sun, Mirror-based multimodal straightforward method for impedance eduction using a zigzag array, J. Sound Vib. 576 (2024) 118237, http://dx.doi.org/10.1016/j.jsv.2024.118237.
[21] W.R. Watson, M.G. Jones, Impedance eduction in large ducts containing high-order modes and grazing flow, in: 23rd AIAA/CEAS Aeroacoustics Conference, 2017, p. 3183, http://dx.doi.org/10.2514/6.2017-3183.
[22] M. Leroux, Propagation acoustique en conduit traité: influence de l'écoulement sur la propagation avec impédance de paroi, [Acoustic propagation in lined duct: flow effects on the propagation in presence of a wall impedance] (Ph.D. thesis), Le Mans, 2005.
[23] J. Golliard, J.-C. Leroux, E. Portier, T. Humbert, Y. Auregan, MAINE flow: Experimental facility for characterization of liners subjected to representative acoustical excitation and grazing flow, in: 25th AIAA/CEAS Aeroacoustics Conference, 2019, p. 2682, http://dx.doi.org/10.2514/6.2019-2682.
[24] J. Golliard, E. Portier, J.-C. Le Roux, T. Humbert, MAINE flow facility for measurement of liner properties in multimodal acoustic field with grazing flow: Qualification and first liner characterization, in: AIAA AVIATION 2021 FORUM, 2021, p. 2145, http://dx.doi.org/10.2514/6.2021-2145.
[25] T. Humbert, J. Golliard, E. Portier, G. Gabard, Y. Auregan, Multimodal characterisation of acoustic liners using the MAINE flow facility, in: 28th AIAA/CEAS Aeroacoustics 2022 Conference, 2022, p. 3082, http://dx.doi.org/10.2514/6.2022-3082.
[26] S. Sack, M. Åbom, C.F. Schram, K. Kucukcoskun, Generation and scattering of acoustic modes in ducts with flow, in: 20th AIAA/CEAS Aeroacoustics Conference, 2014, p. 3115, http://dx.doi.org/10.2514/6.2014-3115.
[27] M. D'Elia, T. Humbert, Y. Aurégan, Effect of flow on an array of Helmholtz resonators: Is Kevlar a ''magic layer''? J. Acoust. Soc. Am. 148 (6) (2020) 3392–3396, http://dx.doi.org/10.1121/10.0002642.
[28] M.E. D'elia, T. Humbert, Y. Aurégan, On articulated plates with micro-slits to tackle low-frequency noise, Acta Acust. 5 (2021) 31, http://dx.doi.org/10.1051/aacus/2021024.
[29] R. Eberhart, J. Kennedy, A new optimizer using particle swarm theory, in: MHS'95. Proceedings of the Sixth International Symposium on Micro Machine and Human Science, IEEE, 1995, pp. 39–43, http://dx.doi.org/10.1109/MHS.1995.494215.